Measurement of (n, γ), (n, p), and $(n, 2n)$ reaction cross sections for sodium, potassium, copper, and iodine at neutron energy 14.92 ± 0.02 MeV with covariance analysis

A. Gandhi ⬤,[*] Aman Sharma, and A. Kumar[†]
Department of Physics, Banaras Hindu University, Varanasi-221005, India

Rebecca Pachuau[‡] and B. Lalremruata ⬤
Department of Physics, Mizoram University, Tanhril, Aizawl-796004, India

S. V. Suryanarayana, L. S. Danu, Tarun Patel ⬤, Saroj Bishnoi, and B. K. Nayak
Bhabha Atomic Research Centre, Mumbai-400085, India

The cross section of the ^{23}Na(n, γ)^{24}Na, ^{41}K(n, p)^{41}Ar, ^{65}Cu(n, p)^{65}Ni, and ^{127}I$(n, 2n)$^{126}I reactions have been measured at 14.92 ± 0.02 MeV neutron energy through neutron activation method followed by off-line γ-ray spectrometry. ^{27}Al(n, α)^{24}Na is used as a reference reaction for the neutron flux normalization. The neutron beam was produced via the ^{3}H(d, n) fusion reaction. Detailed uncertainty propagation has been performed using the covariance analysis and the measured cross sections are being reported with their uncertainties and correlation matrix. The cross sections measured in the present work are compared with the earlier reported cross sections available in the EXFOR database. Furthermore, theoretical calculations have been performed using the EMPIRE-3.2 and TALYS-1.9 codes with RIPL-3 parametrization, from reaction threshold to 20 MeV. The present experimental cross sections are also compared with the evaluated nuclear data from TENDL-2017, JENDL-4.0, and ENDF/B-VIII.0. In the case of (n, γ) and $(n, 2n)$ reactions, the comparison is also made with the IRDFF-1.05 evaluation.

I. INTRODUCTION

Neutron induced reaction cross section data are important in several areas such as accelerator-driven subcritical systems (ADSs), reactors, astrophysics, dosimetry, radiation therapy, and medical applications. The fast neutron induced reaction cross section measurements, in particular, are important for understanding the nuclear phenomena in structural materials irradiated by neutrons. Such data are needed to estimate the nuclear heating, nuclear transmutation rates, induced radioactivity, and for the study of radiation damage effects. Besides its application in the nuclear program, the experimental cross sections are important to test the different statistical model codes and sensitivity of results on the different sets of the parameter used for calculating the cross section [1]. The sodium-potassium (NaK) alloy is one such structural material that is used in the liquid metal fast reactors as a coolant material [2–4]. Also, potassium is present in the cement and concrete walls of the reactors, therefore, its interaction with the fast neutrons gives an impact on the long-term radioprotection, and shielding issues in the nuclear reactor power plant. Sodium and iodine, both are monoatomic and their decay scheme of the resulting nuclide is also well known, and the half-life is of convenient length. The ^{127}I$(n, 2n)$ cross section has been also used as a secondary standard in some experiments [5–8], hence its cross section is of interest. Copper has been chosen for the present study because the material is widely used in the reactor designing and it is one of the important parts of the reactor structural materials. Also, natural copper is used as a shielding material in the detectors for rare event studies like neutrinoless double-β decay [9–13]. With these motivations, we have performed the experiment to measure the fast neutron induced reaction cross sections of the above-mentioned elements. In the paper, we have reported the cross sections of (n, γ), (n, p), and $(n, 2n)$ reactions for ^{23}Na, ^{41}K, ^{65}Cu, and ^{127}I target nuclei at neutron energy 14.92 ± 0.02 MeV. The present measured cross sections with their detailed description of uncertainties are essential for the safety and economy in nuclear applications [14–16]. The present results were compared to the existing cross sections data available in the EXFOR database and evaluated nuclear data from TENDL-2017, IRDFF-1.05, JENDL-4.0, and ENDF/B-VIII.0 [17–22]. We have also employed the latest codes EMPIRE-3.2 and TALYS-1.9 which is based on the Hauser-Feshbach statistical model formalism with different sets of optical model parameters and level density [23,24]. The energy-dependent level density is among the most important input parameter for cross section

---

[*]gandhiaman653@gmail.com
[†]ajaytyagi@bhu.ac.in
[‡]Present address: Department of Nuclear and Atomic Physics, Tata Institute of Fundamental Research, Mumbai-400005, India.

TABLE I. Details of the samples used in the present experiment.

Isotope	Sample irradiated	Abundance of isotope (%)	Weight of sample (mg)	Thickness (mm)	Number of atoms of the isotope in sample (10^{-4} atoms/barn)
^{23}Na	Na_2CO_3 powder	100	570.0 ± 0.1	4	64.78
^{41}K	K_2SO_4 powder	6.7302 ± 0.0044	370.5 ± 0.1	2	1.612
^{65}Cu	Cu metal sheet	30.85 ± 0.15	116.5 ± 0.1	0.125	3.330
^{127}I	KI powder	100	91.0 ± 0.1	2	3.280
^{27}Al	Al foil	100	22.5 ± 0.1	0.025	5.019

calculation in the nuclear reaction models. Although both codes in principle are using RIPL-3 parametrization for adjustment of the level density, however EMPIRE did not adopt the RIPL-3 Bardeen-Cooper-Schrieffer (BCS) and Gilbert Cameron (GC) parametrization. An accurate and reliable description of the excited levels of the nucleus is necessary for testing the quality of the reaction model used for the calculation of cross section [25–28]. The motivation for doing these theoretical model calculations was to reproduce the best-estimated results compared to the present measured cross sections and existing experimental data reported in EXFOR database [17,18].

II. EXPERIMENTAL DETAILS

A. Neutron source

The experiment was performed using the Cockcroft and Walton type accelerator, Purnima facility at Bhabha Atomic Research Centre (BARC), Mumbai [29]. The neutron beam was generated through the $d + ^3\text{H} \rightarrow n + ^4\text{He}$ reaction (Q value = 17.589 MeV). In the present experiment, the D^+ ions were accelerated to the 140 ± 5 keV and bombarded on the Ti-T target producing the neutron beam of energy 14.92 ± 0.02 MeV at zero degree. The average deuteron beam current was 60 μA during sample irradiation.

B. Sample preparation

The activation samples of sodium, potassium, iodine were in the form of pellets while copper was used as a thin metal sheet. A pure chemical compound of sodium, potassium, and iodine has been used in the powder form and a known amount of it was pressed in pellet having a circular shape of diameter 1 cm packed into the polyethylene bag. For the copper irradiation, we have used the square shape Cu metal sheet (99.99% pure of grade-1) of size 1×1 cm^2 wrapped in pure aluminium foil. The aluminium foil has been used for the normalization of the neutron flux using the ^{27}Al(n, α)^{24}Na reference reaction cross section taken from the IRDFF-1.05 library, which is a standard library for the monitor reaction cross section [20]. More details about the samples used in the experiment are given in Table I. The samples were weighed using a microbalance machine which had the least count of 0.1 mg. Irradiation of all samples was taken together by making the stack of Al-Cu-Na-K-I mounted at zero degree with respect to the beam direction at a distance 11 mm from the Ti-T target covering an angle of 26.03°. The angular coverage of the neutron beam was about 10°, thus according

to the reaction kinematics, the neutrons impinging on the samples were monoenergetic [30].

C. Gamma ray spectrometry

After completion of the neutron irradiation, the radioactive samples were taken out from the irradiation room and then cooled. Since different elements used in this experiment have different neutron cross sections and different half-lives, it requires an optimum time for the irradiation of all the samples. This irradiation time varies according to the irradiated elements, but will always be below the saturation point. Similarly, the cooling period selected for various samples, allows the short-lived radioactive species that might interfere with the analyzed element to decay before counting the desired γ rays. The details of the irradiation, cooling, and counting times are given in Table II. The irradiated samples were mounted on different perplex plates and then taken to the counting room. The induced activity on the samples and reference foil were measured using a precalibrated lead-shielded 185-cc high purity germanium detector (HPGe) having 30% relative efficiency and 1.8 keV energy resolution at 1.33 MeV γ-ray energy. The data acquisition was carried out using the CAMAC-based Linux Advanced Multi-parameter System LAMPS Software (TCAMCON-95/CC 2000 crates controller and CM-48 ADCs) and the detector dead time was negligible. The details of the nuclear decay data and their uncertainties used in the present experiment are given in Table III.

The efficiency calibration of the HPGe detector for different characteristic γ-ray energies has been determined using a standard ^{152}Eu point source ($T_{1/2} = 13.517 \pm 0.009$ y [35]), of known activity ($A_0 = 6659.21 \pm 81.60$ Bq as on 1 Oct. 1999). The absolute efficiency of the point source placed at a distance of 2 mm from the detector absorber was determined by

$$\varepsilon_p = \frac{CK_c}{A_0 I_\gamma e^{-\lambda t} \Delta t}, \tag{1}$$

TABLE II. Irradiation, cooling, and counting times.

Reaction	Irradiation time (sec)	Cooling time (sec)	Counting time (sec)
^{23}Na(n, γ)^{24}Na	8525	90763	8151
^{41}K(n, p)^{41}Ar	8525	14361	3092
^{65}Cu(n, p)^{65}Ni	8525	11268	2030
^{127}I$(n, 2n)$^{126}I	8525	595276	7555
^{27}Al(n, α)^{24}Na	8525	11268	2030

TABLE III. Nuclear decay data and their uncertainties used in the present experiment.

Reaction	Product nuclide	Threshold energy (keV)	Half-life ($t_{1/2}$)	E_γ (keV)	I_γ (%)	Reference
^{23}Na(n, γ)	^{24}Na	0.00	14.997 $\pm$ 0.012 h	1368.62	99.9936 $\pm$ 0.0015	[31]
^{41}K(n, p)	^{41}Ar	1751.80	109.61 $\pm$ 0.04 min	1293.64	99.16 $\pm$ 0.02	[32]
^{65}Cu(n, p)	^{65}Ni	1376.69	2.5175 $\pm$ 0.0005 h	1481.84	23.59 $\pm$ 0.14	[33]
^{127}I$(n, 2n)$	^{126}I	9216.60	12.93 $\pm$ 0.05 d	666.33	32.9 $\pm$ 0.7	[34]
^{27}Al(n, α)	^{24}Na	3249.69	14.997 $\pm$ 0.012 h	1368.62	99.9936 $\pm$ 0.0015	[31]

where A_0 is the activity of ^{152}Eu point source at the time of manufacturing, C is the number of counts during the counting time ($\Delta t = 2632$ s), for a particular γ-ray energy of interest with absolute intensity ($I\gamma$). The elapsed time (t) is the time between the date of manufacturing to the date of counting and (K_c) is the summing correction factor. By placing the source at 2 mm distance from the detector absorber, introduces a coincidence summing effect and, hence, the correction has to be made for the detector efficiency measurement. Since our samples have a finite area, therefore the efficiency for the point source geometry (ε_p) was transferred to the efficiency for sample geometry (ε) by using the Monte Carlo simulation code EFFTRAN and the same code also has been used to calculate the coincidence-summing correction factor (K_c) [36,37]. The obtained efficiency values for the characteristic γ-ray energies of ^{152}Eu are given in Table IV and plotted in Fig. 1. The detector efficiency for the characteristic γ-ray energy of the product nuclide was obtained by interpolating the point-wise efficiencies of the γ-ray energies (E_γ) given in Table IV through the fitting function given by

$$\varepsilon(E_\gamma) = \varepsilon_o \exp(-E_\gamma/E_0) + \varepsilon_c, \qquad (2)$$

where three parameters (ε_c, ε_o, and E_0) are determined by fitting the above function to the measured detection efficiencies (ε) of ^{152}Eu point source with their uncertainties propagated from different attributes, i.e., ΔC, $\Delta I\gamma$, ΔA_0, and

$\Delta \lambda$. The fitting parameter values are given in Table V with its uncertainty and the correlation matrix, which are further used to obtain the covariance between interpolated detection efficiencies [38,39].

The covariance between interpolated detection efficiencies was determined by equation 38 of Ref. [14]. The detection efficiency of the characteristic γ-ray energies of the product nuclide with its uncertainty and correlation matrix is given in Table VI.

D. Estimation of the activation cross section and its uncertainty

In the present work, the activation cross sections were derived with the ^{27}Al(n, α) ^{24}Na reference monitor cross section using the well-known standard neutron activation equation given by

$$\sigma_s = \sigma_{Al} \frac{A_s \lambda_s a_{Al} N_{Al} I_{\gamma(Al)} \varepsilon_{Al} f_{Al}}{A_{Al} \lambda_{Al} a_s N_s I_{\gamma(s)} \varepsilon_s f_s} \times \frac{C_{attn.(s)}}{C_{attn.(Al)}}, \qquad (3)$$

where (σ_{Al}) is the reference monitor cross section of ^{27}Al(n, α) ^{24}Na reaction at a neutron energy 14.92 ± 0.02 MeV obtained by the linear interpolation method by considering the cross section values at the nearest energy points taken from IRDFF-1.05, which is obtained as 0.1092 ± 0.000398 b [20], (A) is the photopeak counts of the characteristic γ ray of the product nuclide having absolute intensity (I_γ), (λ) is the decay constant, (a) is the isotopic abundance of the target nuclei, (N) is the number of atoms, and (ε) is the HPGe detector efficiency of the characteristic γ ray of the product nuclide. The timing factor (f) of the samples and the Al monitor is given by

$$f = (1 - e^{-\lambda t_{irr}}) e^{-\lambda t_{cool}} (1 - e^{-\lambda t_{count}}), \qquad (4)$$

where (t_{irr}) is the irradiation time, (t_{cool}) is the cooling time, and (t_{count}) is the counting time. ($C_{attn.}$) is the correction factor for γ-ray self-attenuation applied to the measured cross section [40–42]. The correction factor for self-attenuation of γ-ray fluxpassingthrough a sample of thickness (d) with mass attenuation coefficient of the γ-ray energy and material (μ_m) was determined using the formula

$$C_{attn.} = \frac{\mu_m d}{1 - \exp(-\mu_m d)}, \qquad (5)$$

where (μ_m) is calculated from the XMuDat version 1.0.1 [43] and the obtained correction factor for γ-ray self-attenuation of different samples is given in Table VII.

The uncertainty propagation in the measured cross sections was done by considering the fractional uncertainty in various
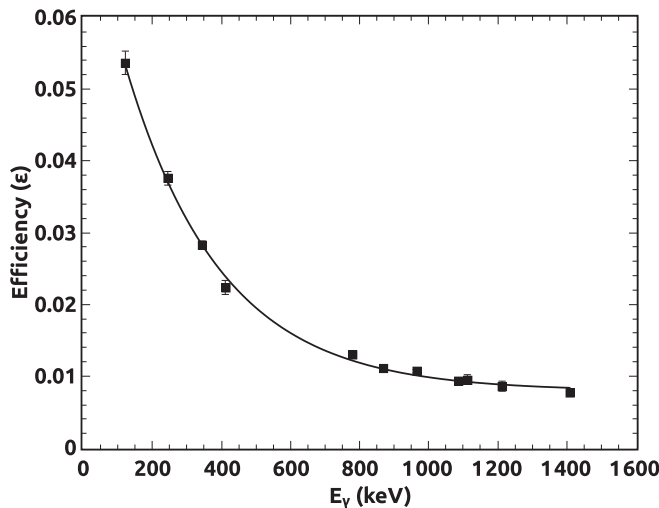

FIG. 1. Efficiency calibration curve of the HPGe detector for the sample geometry source placed at a distance of 2 mm from the top of detector absorber.

TABLE IV. HPGe detector efficiency for the point source (ε_p) with sample shape geometry (ε) at the characteristic γ-ray energies of ^{152}Eu with γ-ray intensities taken from ENSDF [35] and correction factor (K_c) for coincidence summing effect.

E_γ (keV)	I_γ	Counts (C)	K_c	ε_p	ε
121.78	0.2853 ± 0.0016	186555.4 ± 5118.3	1.165	0.053694	0.053318 ± 0.001630
244.69	0.0755 ± 0.0004	32729.2 ± 710.5	1.230	0.037583	0.037320 ± 0.000951
344.27	0.2659 ± 0.0020	95780.1 ± 1417.3	1.113	0.028258	0.028060 ± 0.000579
411.11	0.02238 ± 0.00013	5512.2 ± 231.0	1.288	0.022360	0.022203 ± 0.000978
778.90	0.1293 ± 0.0008	20438.3 ± 308.7	1.165	0.012979	0.012888 ± 0.000263
867.38	0.0423 ± 0.0003	5259.4 ± 178.7	1.274	0.011165	0.011086 ± 0.000408
964.05	0.1451 ± 0.0007	20001.3 ± 317.4	1.099	0.010677	0.010602 ± 0.000218
1085.83	0.1011 ± 0.0005	14414.6 ± 761.5	0.925	0.009295	0.009230 ± 0.000502
1112.94	0.1367 ± 0.0008	17657.6 ± 1248.9	1.045	0.009514	0.009447 ± 0.000680
1212.94	0.01415 ± 0.00008	1362.8 ± 79.1	1.265	0.008587	0.008527 ± 0.000508
1408.01	0.2087 ± 0.0009	21291.8 ± 391.1	1.069	0.007687	0.007633 ± 0.000171

attributes, i.e., timing factor (f_s, f_{Al}), efficiency (ε_s, ε_{Al}), γ-ray intensity ($I_{\gamma(s)}$, $I_{\gamma(\text{Al})}$), isotopic abundance of the sample nuclei (a_s), number of atoms (N_s, N_{Al}), γ-ray photopeak counts (A_s, A_{Al}) and monitor reaction cross section (σ_{Al}). For the case of ^{23}Na, ^{127}I, and ^{27}Al target nuclei, the fractional uncertainty from the isotopic abundance has been omitted as these isotopes have 100% isotopic abundance. The fractional uncertainty in the timing factor (f) was estimated by following Sec 4.1.3 of Ref. [14].

E. Covariance analysis

Covariance analysis is a mathematical tool which can help to describe the detailed uncertainties with cross-correlation among different measured quantities. Many areas of experimental nuclear science have become highly quantitative in nature and one of such experimental quantitative science is nuclear data, having applications, ranging from the design of fission and fusion reactors to nuclear medicine. Therefore, investigations which produce such kinds of quantitative information and has such an applied impact, have an obligation to perform the experiment carefully and to report the experimental investigation in details, that includes the experimental uncertainties and its covariance matrix. This detailed information helps the evaluator to do the evaluation process of the nuclear data precisely and correctly. In the present work, different reactions cross section have been measured at a neutron energy 14.92 ± 0.02 MeV and as the counting of all the irradiated samples has been done with the same detector system, therefore all the reaction cross sections are correlated with the efficiency of the detector. Besides, the counts from the recorded γ-ray spectra, various other parameters with def-

inite uncertainties were also taken into consideration for the calculation of uncertainty in measured cross sections and its covariance matrix. The fractional uncertainties from all these parameters and the correlation coefficient between different reaction cross section are summarized in Table VIII. The correlation coefficient of two parameters (x_1, x_2) is represented as uncorrelated [$\text{Cor}(x_1, x_2) = 0$] and fully correlated coefficient [$\text{Cor}(x_1, x_2) = 1$]. However, the numerical value of the correlation coefficient must be between -1 to $+1$ [14–16]. From these fractional uncertainties and correlation coefficient given in Table VIII, we have constructed the fractional variance and covariance by following Sec 4.1.4 of Ref. [14]. The results of measured reaction cross sections with their uncertainties and correlation matrix are presented in Table IX.

III. THEORETICAL CALCULATIONS

The theoretical calculations for ^{23}Na(n, γ)^{24}Na, ^{41}K(n, p)^{41}Ar, ^{65}Cu(n, p)^{65}Ni, and ^{127}I$(n, 2n)$I^{126} reactions have been done at neutron energies from reaction threshold to 20 MeV by using the statistical nuclear reaction model codes EMPIRE-3.2 and TALYS-1.9 [23,24]. The calculations are based on different mechanisms of the nuclear reactions which vary with the incident energy. These codes take into account the three major reaction mechanisms that include direct reaction (DI), pre-equilibrium emission (PE), and compound nucleus (CN). To estimate contributions from all such mechanisms, the codes incorporate various nuclear models that use the different sets of optical model parameters and level density. The contribution from all the three mechanisms makes the total reaction cross section. In the present defined energy range, the maximum contribution comes from the compound nucleus process followed by the pre-equilibrium emission and direct reaction. The theoretical calculations are done by using the optimum combination of input parameters and their values defined for different models and parameters that reproduce the most satisfactory results compared to the present experimental data and all the available existing experimental data reported in the EXFOR database. The calculated cross section results are also compared with the evaluated nuclear data from IRDFF-1.05, TENDL-2017, JENDL-4.0, and ENDF/B-VIII.0.

TABLE V. Efficiency (ε) curve fitting parameter values with its uncertainty and correlation matrix.

Parameters	Value	Uncertainty	Correlation matrix		
ε_c	0.00792	3.67958×10^{-4}	1.0000		
ε_0	0.07047	0.0029	0.4765	1.0000	
E_0 (keV)	277.11562	14.62125	-0.7741	-0.8365	1.0000

TABLE VI. Interpolated detector efficiency of the characteristic γ ray of the product nuclide with its uncertainty and correlation matrix.

Reaction	E_γ(keV)	Efficiency	Correlation matrix				
^{23}Na$(n, \gamma)^{24}$Na	1368.62	0.00842 ± 0.00028	1.0000				
^{41}K$(n, p)^{41}$Ar	1293.64	0.00858 ± 0.00026	0.9972	1.0000			
^{65}Cu$(n, p)^{65}$Ni	1481.84	0.00825 ± 0.00036	0.9969	0.9882	1.0000		
^{127}I$(n, 2n)^{126}$I	666.33	0.01428 ± 0.00036	-0.1316	-0.0581	-0.2078	1.0000	
^{27}Al$(n, \alpha)^{24}$Na	1368.62	0.00842 ± 0.00028	1.0000	0.9972	0.9969	-0.1316	1.0000

A. EMPIRE-3.2 calculation

The EMPIRE-3.2 code was used for estimating the cross section of ^{23}Na$(n, \gamma)^{24}$Na, ^{41}K$(n, p)^{41}$Ar, ^{65}Cu$(n, p)^{65}$Ni, and ^{127}I$(n, 2n)$I^{126} reactions over the neutron energy range from reaction threshold to 20 MeV. In EMPIRE, the description of compound level density parameters was carried out according to the Gilbert-Cameron model, parametrized by Ijinov *et al.* [44] for the capture reaction cross section (*LEVDEN 2*) and enhanced generalized superfluid model formalism for other reaction channels (*LEVDEN 0*), while the contribution from the direct reaction and the transmission coefficients were calculated by the spherical optical model using the ECIS-06 code with the global optical model potential, proposed by Koning and Delaroche for n and p, taken from RIPL-3 library nos. 2405 and 5405, respectively [45,46]. The statistical Hauser-Feshbach model is used for calculating the compound nucleus contribution. For pre-equilibrium emission, the classical exciton model was used by means of the PCROSS code that calculates the pre-equilibrium contribution with default mean free path multiplier (*PCROSS 1.5*). For the γ transmission coefficients, EMPIRE offers different γ strength functions, and in the present case, we have used the SLO (standard Lorentzian) for the capture reaction cross section and EGLO (enhanced generalized Lorentzian) (Uhl-Kopecki) function for other reactions. To fit the theoretical results of the capture reaction cross section with the measured cross section, we have done the tuning of the compound nucleus and pre-equilibrium emission parameter by setting up the TUNEPE (*for pre-equilibrium emission*) parameter value to 5 and the global TUNE (*for compound nucleus*) value to 2, respectively. These adjustable parameters are nonphysical parameters in the EMPIRE code which are designed to be used in nuclear data evaluation to correct the reaction model deficiencies.

B. TALYS-1.9 calculation

The TALYS-1.9 code has been also used for the analysis and estimation of a nuclear reaction cross section. The code works for the reactions that involve neutrons, photons, protons, deuterons, tritons, and ^{3}He particles as an incident particle in the energy range from 1 keV–200 MeV and for target nuclides of mass 12 and heavier. To achieve this, TALYS implemented a suite of nuclear reaction models into a single code system which enables us to evaluate nuclear reactions from the unresolved resonance range up to the intermediate energies. TALYS generates nuclear data for all open reaction channels, on user-defined energy and angle grid, beyond the resonance region. The default set of input parameters have been used in which the optical model parameters for neutrons and protons were obtained by a local potential proposed by Koning and Delaroche [45].

The distorted wave Born approximation (DWBA) model has been used for the direct reaction contribution and the calculation was done by means of the ECIS-06 code [47,48]. The two-component exciton model developed by Kalbach was used for calculating the pre-equilibrium emission contribution, and the compound nucleus contribution was calculated by the Hauser-Feshbach statistical model with width model correction using the Moldauer model [49–51]. The enhanced generalized Lorentzian model (Uhl-Kopecki) was used for γ-ray strength functions for the incident neutron. To calculate the compound level density parameters we have used the constant temperature and Fermi gas model (*ldmodel 1*) and Microscopic level densities (Skyrme force) from Goriely's tables (*ldmodel 4*). For fitting of the neutron capture cross section with the present measured cross section, an adjustable parameter (*gnorm* = 5) has been used which is a normalization factor for γ-ray transmission coefficient. This adjustable parameter was used to scale the (n, γ) cross sections. The input parameters required in nuclear models for cross section calculation such as the nuclear masses, discrete levels and decay schemes, neutron resonances, optical model parameters, level densities, γ-ray strength function, and fission barriers are taken from the RIPL-3 library [46].

The results of the theoretical calculations for all the reactions are presented in the following section, along with the present measured cross sections wand existing cross sections data from the EXFOR database.

TABLE VII. γ-ray self-attenuation correction factor ($C_{\text{attn.}}$) applied to the measured cross section.

Sample	Na$_2$CO$_3$	K$_2$SO$_4$	Cu	KI	Al
E_γ (keV)	1368.62	1293.64	1481.84	666.33	1368.62
$C_{\text{attn.}}$	1.0271	1.0150	1.0027	1.0240	1.0002

TABLE VIII. Fractional uncertainties (%) from different parameter associated with the measured cross section and the correlation coefficient between different reaction cross section measured at 14.92 ± 0.02 MeV neutron energy.

Reaction	(x)	f_s	f_{Al}	ε_s	ε_{Al}	I_s	I_{Al}	σ_{Al}	a_s	N_s	N_{Al}	A_s	A_{Al}	Total error (%)
^{23}Na$(n,\gamma)^{24}$Na	(1)	0.0466	0.0054	3.3254	3.3254	0.0015	0.0015	0.3644	–	0.0175	0.4444	5.1784	1.1314	7.1095
^{41}K$(n,p)^{41}$Ar	(2)	0.0088	0.0054	3.0303	3.3254	0.0201	0.0015	0.3644	0.0653	0.0269	0.4444	2.3291	1.1314	5.2232
^{65}Cu$(n,p)^{65}$Ni	(3)	0.0042	0.0054	4.3636	3.3254	0.5934	0.0015	0.3644	0.4862	0.0858	0.4444	4.3848	1.1314	7.1785
^{127}I$(n,2n)^{126}$I	(4)	0.1174	0.0054	2.5210	3.3254	2.1276	0.0015	0.3644	–	0.1098	0.4444	1.3001	1.1314	5.0266
Correlation	Cor(1,1)	1	1	1	1	1	1	1	1	1	1	1	1	1.0000
coefficient	Cor(1,2)	0	1	0.9972	1	0	1	1	0	0	1	0	1	0.6118
	Cor(1,3)	0	1	0.9969	1	0	1	1	0	0	1	0	1	0.5317
	Cor(1,4)	0	1	-0.1316	1	0	1	1	0	0	1	0	1	0.3236
	Cor(2,2)	1	1	1	1	1	1	1	1	1	1	1	1	1.0000
	Cor(2,3)	0	1	0.9882	1	0	1	1	0	0	1	0	1	0.6864
	Cor(2,4)	0	1	-0.0581	1	0	1	1	0	0	1	0	1	0.4656
	Cor(3,3)	1	1	1	1	1	1	1	1	1	1	1	1	1.0000
	Cor(3,4)	0	1	-0.2078	1	0	1	1	0	0	1	0	1	0.2877
	Cor(4,4)	1	1	1	1	1	1	1	1	1	1	1	1	1.0000

IV. RESULTS AND DISCUSSION

The ^{23}Na$(n,\gamma)^{24}$Na, ^{41}K$(n,p)^{41}$Ar, ^{65}Cu $(n, p)^{65}$Ni, and ^{127}I$(n, 2n)$I^{126} reaction cross sections measured at neutron energy 14.92 ± 0.02 MeV with their uncertainties and correlation matrix are presented in Table IX. The measured cross sections deduced in the present work are plotted in Figs. 2–5 along with the already existing experimental data reported in the EXFOR database. Also, the present results are compared with the evaluated nuclear data from TENDL-2017, IRDFF-1.05, JENDL-4.0, and ENDF/B-VIII.0 and the nuclear reaction model codes EMPIRE-3.2 and TALYS-1.9. The present experimental data are shown as a solid rectangular shape in red color while the different symbols, as explained in the figures, are used to represent existing data in EXFOR database (with error bar taken only along the y axis). The theoretically calculated excitation functions from EMPIRE-3.2 and TALYS-1.9 are shown as solid black and red line respectively, and TENDL-2017, IRDFF-1.05, JENDL-4.0, and ENDF/B-VIII.0 evaluated data are shown by dash-dash (olive color), dot-dot (sky blue color), dash-dot-dash (pink color), and dash-dot-dot-dash (blue color) lines, respectively. These specific notations are followed throughout this paper. The contribution from different reaction mechanisms in total reaction cross section also have been presented in Figs. 6–9.

A. The ^{23}Na$(n, \gamma)^{24}$Na reaction

In Fig. 2, we have plotted the obtained cross section of ^{23}Na$(n, \gamma)^{24}$Na reaction together with TALYS-1.9 and EMPIRE-

3.2 theoretical calculations. In addition to the measured data, we have included seven sets of existing experimental data available in EXFOR in the energy range up to 20 MeV. It is clear from Fig. 2, that the measurement around 14 MeV region is showing discrepancy between the data measured by different groups. The present measured cross section is found in agreement with the cross section data reported by Menlove *et al.* [52] within the experimental uncertainty. The theoretically calculated cross sections has taken a good account with the present measured data and the trend of theoretical results are consistent with the existing data and evaluated data up to 16 MeV. However, above 16 MeV the theoretically predicted results overestimate the existing data and are not consistent with the evaluations. To validate the theoretical results above 16 MeV new measurements are required. In the present energy range, the contribution from the compound nucleus and pre-equilibrium emission is dominant than the direct reaction contribution in ^{23}Na$(n, \gamma)^{24}$Na total cross section as shown in Fig. 6.

B. The ^{41}K$(n, p)^{41}$Ar reaction

In Fig. 3, we have plotted the measured cross section of ^{41}K$(n, p)^{41}$Ar reaction with the literature data, evaluated data, and theoretically calculated results. In Fig. 3, the theoretical results and TENDL-2017 evaluations are in good agreement with our obtained cross section result, and also consistent with the existing data from the EXFOR database within the uncertainty limit. However, the evaluated data

TABLE IX. The measured reaction cross sections with their uncertainties and correlation matrix.

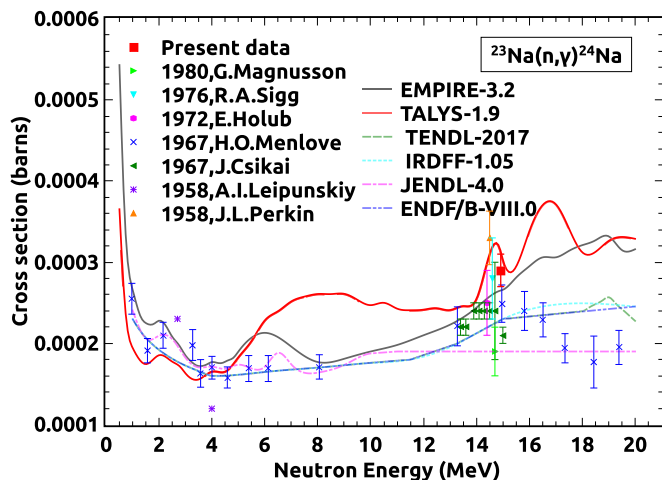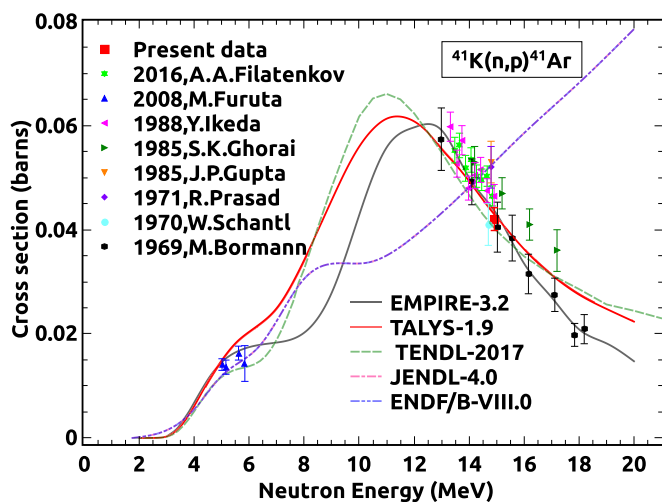| Reaction	Cross section (b) $(\sigma \pm \triangle \sigma)$	Correlation matrix			
^{23}Na$(n, \gamma)^{24}$Na	0.00029 ± 0.00002	1.0000			
^{41}K$(n, p)^{41}$Ar	0.04204 ± 0.00219	0.6118	1.0000		
^{65}Cu$(n, p)^{65}$Ni	0.02244 ± 0.00161	0.5317	0.6864	1.0000	
^{127}I$(n, 2n)^{126}$I	1.51848 ± 0.07632	0.3236	0.4656	0.2877	1.0000

FIG. 2. Cross section of $^{23}\text{Na}(n, \gamma)^{24}\text{Na}$ reaction measured in present work and comparative studies with the existing experimental cross section data at different neutron energies with EMPIRE-3.2 and TALYS-1.9 as well as the evaluated data.
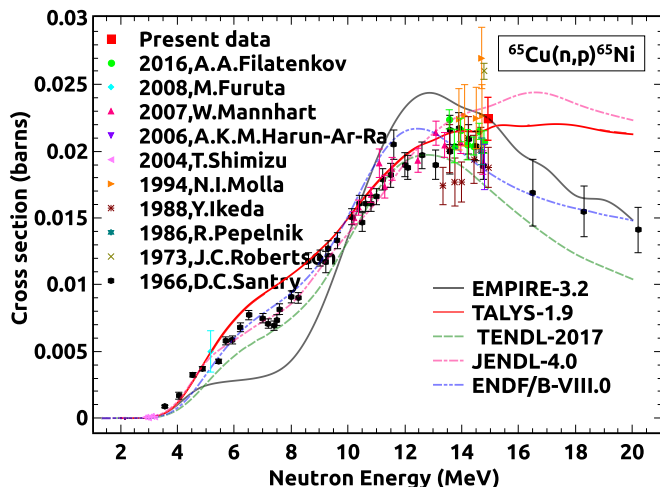

FIG. 4. Cross section of $^{65}\text{Cu}(n, p)^{65}\text{Ni}$ reaction measured in present work and comparative studies with the existing experimental cross section data at different neutron energies with EMPIRE-3.2 and TALYS-1.9 as well as the evaluated data.

JENDL-4.0 and ENDF/B-VIII.0 are inconsistent with the existing experimental data and theoretical estimated results. For $^{41}\text{K}(n, p)^{41}\text{Ar}$ reaction, the maximum contribution comes from the compound nucleus process followed by the pre-equilibrium emission and direct reaction mechanism as shown in Fig. 7.

C. The $^{65}\text{Cu}(n, p)^{65}\text{Ni}$ reaction

The measured excitation function for the reaction $^{65}\text{Cu}(n, p)^{65}\text{Ni}$ is shown in Fig. 4 along with the existing data in the energy range from reaction threshold to 20 MeV. It is clear from Fig. 4, that plenty of measurements exist in the neutron energy range from 12 MeV to 15 MeV and the

result obtained from the present measurement is consistent with the existing data. Theoretically calculated results from EMPIRE-3.2 and TALYS-1.9 codes are also in good agreement with the present measurement and following the trend of experimental data and with the TENDL-2017 and ENDF/B-VIII.0 evaluated data. However, above 15 MeV, the TALYS and JENDL-4.0 evaluated results overestimate the experimental data reported by Santry *et al.* [53]. The contribution from different reaction mechanisms in $^{65}\text{Cu}(n, p)^{65}\text{Ni}$ is shown in Fig. 8 and it is observed that at energy above 8 MeV, the effect of pre-equilibrium emission increases with energy and it is equally contributing in the present reaction cross section as

FIG. 3. Cross section of $^{41}\text{K}(n, p)^{41}\text{Ar}$ reaction measured in present work and comparative studies with the existing experimental cross section data at different neutron energies with EMPIRE-3.2 and TALYS-1.9 as well as the evaluated data.
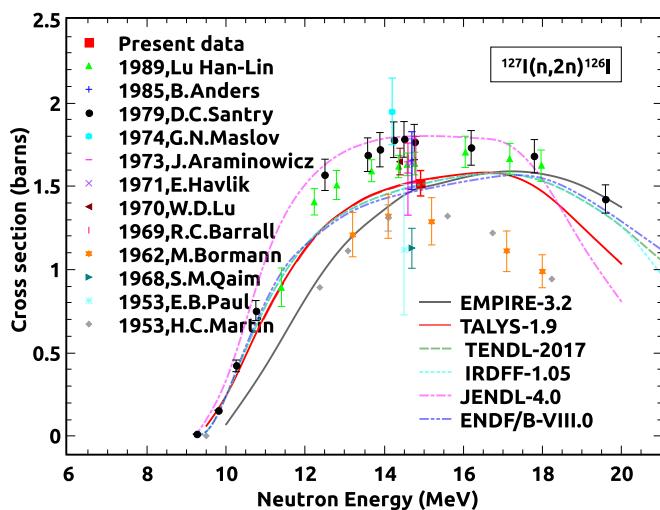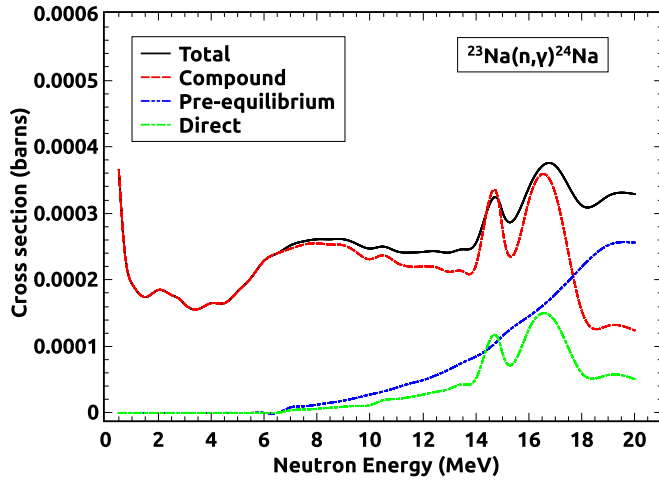

FIG. 5. Cross section of $^{127}\text{I}(n, 2n)^{126}\text{I}$ reaction measured in present work and comparative studies with the existing experimental cross section data at different neutron energies with EMPIRE-3.2 and TALYS-1.9 as well as the evaluated data.
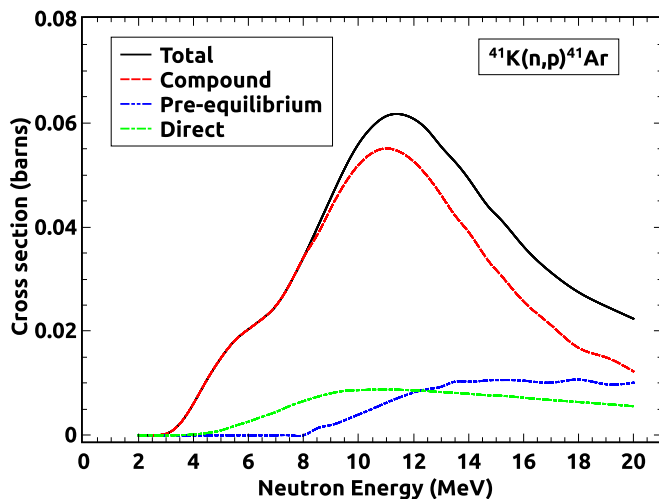
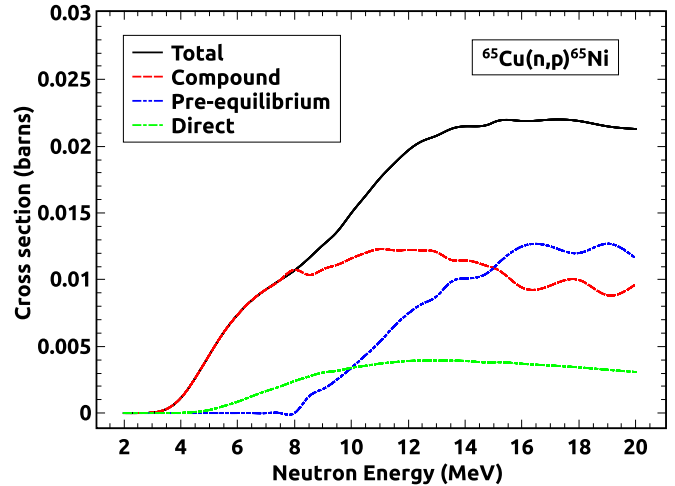FIG. 6. Contribution from different reaction mechanisms in total ^{23}Na(n, γ) ^{24}Na reaction cross section.

FIG. 8. Contribution from different reaction mechanisms in total ^{65}Cu(n, p) ^{65}Ni reaction cross section.

from the compound nucleus process with a minor contribution from the direct reaction.

D. The ^{127}I$(n, 2n)$ ^{126}I reaction

The measured and theoretical calculated cross section for ^{127}I$(n, 2n)$ ^{126}I reaction is plotted in Fig. 5 together with the available literature data and evaluated data. The theoretical estimated results are in good agreement with the present measured cross section and the trend of theoretical results are consistent with the TENDL-2017, IRDFF-1.05, and ENDF/B-VIII.0 evaluations. However, the JENDL-4.0 evaluation overestimates the present measured data and theoretical results. While, the TENDL-2017, IRDFF-1.05, and ENDF/B-VIII.0 evaluated data are consistent with the present experimental result. For the present $(n, 2n)$ reaction, the contribution from the pre-equilibrium emission and direct reaction mechanisms

are negligible in comparison to the compound nucleus process in total reaction cross section as shown in Fig. 9.

V. SUMMARY AND CONCLUSION

Neutron induced reaction cross section for ^{23}Na(n, γ) ^{24}Na, ^{41}K(n, p) ^{41}Ar, ^{65}Cu(n, p) ^{65}Ni, and ^{127}I$(n, 2n)$ ^{126}I reactions have been measured using the latest nuclear decay data at neutron energy 14.92 ± 0.02 MeV, relative to the ^{27}Al(n, α) ^{24}Na reaction reference cross section using the method of neutron activation followed by off-line γ-ray spectrometry. The experiment was performed using the ^{3}H(d, n) fusion reaction based neutron generator at Purnima facility, BARC, Mumbai. Detailed covariance analysis has been performed to estimate the measured cross section uncertainties and the correlation matrix between different reaction cross sections. The uncertainties in the measured cross sections are found in the range of $\approx$5–7%. The present experimental cross sections are in good agreement with
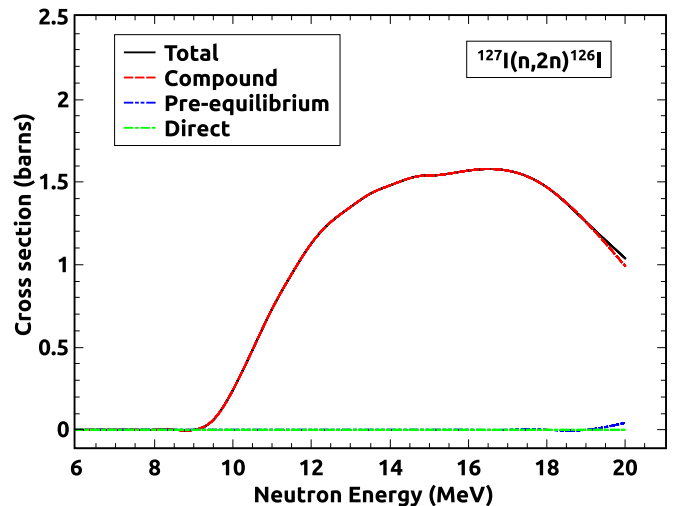

FIG. 7. Contribution from different reaction mechanisms in total ^{41}K(n, p) ^{41}Ar reaction cross section.

FIG. 9. Contribution from different reaction mechanisms in total ^{127}I$(n, 2n)$ ^{126}I reaction cross section.

the literature data as well as with the evaluated nuclear data from TENDL-2017, IRDFF-1.05, JENDL-4.0, and ENDF/B-VIII.0. In addition, the present measured cross sections also have been reproduced using the theoretical nuclear reaction model codes EMPIRE-3.2 and TALYS-1.9, and both codes reproduced fairly well the measured cross sections and the existing cross section data reported in the EXFOR database. Also, it is observed that the effect of pre-equilibrium emission is major in (n, p) reactions compared to the $(n, 2n)$ reaction cross sections. The present experimental results with detailed covariance information are important for verification of nuclear reaction codes and other applications in the nuclear technology development.

[1] L. A. Bernstein *et al.*, Annu. Rev. Nucl. Part. Sci. **69**, 109 (2019).
[2] C. Wang *et al.*, Prog. Nucl. Energy **68**, 142 (2013).
[3] F. Arbeiter *et al.*, Nucl. Mater. Energy **9**, 59 (2016).
[4] A. lbarra *et al.*, Fusion Sci. Technol. **66**, 252 (2014).
[5] S. J. Bame, Jr. and R. L. Cubitt, Phys. Rev. **113**, 256 (1959).
[6] R. L. Macklin, N. H. Lazar, and W. S. Lyon, Phys. Rev. **107**, 504 (1957).
[7] R. Booth, W. P. Ball, and M. H. MacGregor, Bull. Am. Phys. Soc. Ser. II **2**, 268 (1957).
[8] A. E. Johnsrud, M. G. Silbert, and H. H. Barschall, Bull. Am. Phys. Soc. Ser. II **3**, 165 (1958).
[9] I. Newsome, M. Bhike, Krishichayan, and W. Tornow, Phys. Rev. C **97**, 044617 (2018).
[10] J. Albert (EXO-200 Collaboration) *et al.*, Nature **510**, 229 (2014).
[11] A. Branca (CUORE Collaboration) *et al.*, arXiv:1705.00005v2 (2016).
[12] C. Alduino (CUORE Collaboration) *et al.*, Phys. Rev. Lett. **120**, 132501 (2018).
[13] M. Agostini (GERDA Collaboration) *et al.*, Nature **544**, 47 (2017).
[14] N. Otuka *et al.*, Radiat. Phys. Chem. **140**, 502 (2017).
[15] W. Mannhart, International Atomic Energy Agency Report No. INDC(NDS)-0588 (Rev.) (2013).
[16] D. L. Smith, Nucl. Instrum. Methods Phys. Res. A **257**, 365 (1987).
[17] N. Otuka *et al.*, Nucl. Data Sheets **120**, 272 (2014).
[18] EXFOR database, https://www-nds.iaea.org/exfor/ (Data retrieved on date January 2020).
[19] A. J. Koning and D. Rochman, Nucl. Data Sheets **113**, 2841 (2012).
[20] E. M. Zsolnay, R. Capote, H. K. Nothenius, and A. Trkov, Technical Report No. INDC(NDS)-0616, IAEA, Vienna (2012).
[21] K. Shibata *et al.*, J. Nucl. Sci. Technol. **48**, 1 (2011).
[22] A. David Brown *et al.*, Nucl. Data Sheets **148**, 1 (2018).
[23] M. Herman *et al.*, EMPIRE-3.2 Malta modular system for nuclear reaction calculations and nuclear data evaluation Users Manual, No. BNL [101378-2013]. Brookhaven National Laboratory (BNL) National Nuclear Data Center (2013).
[24] A. J. Koning, S. Hilaire, and M. C. Duijvestijn, in TALYS-1.0, *Proceedings of the International Conference on Nuclear Data for Science and Technology, April 22–27, 2007, Nice, France,* edited by O. Bersillon, F. Gunsing, E. Bauge, R. Jacqmin, and S. Leray (EDP Sciences, Les Ulis, France, 2008), p. 211.
[25] B. Canbula, Nucl. Instrum. Methods Phys. Res. B **391**, 73 (2017).
[26] J. Luo and L. Jiang, Eur. Phys. J. A **55**, 27 (2019).
[27] A. Gandhi *et al.*, Indian J. Phys. **93**, 1345 (2019).
[28] A. Gandhi *et al.*, J. Radiol. Nucl. Chem. **322**, 89 (2019).
[29] A. Sinha *et al.*, Nucl. Instrum. Methods Phys. Res. B **350**, 66 (2015).
[30] L. Kicka, Characterization of neutron fields around an intense neutron generator, doctoral dissertation (2016).
[31] R. B. Firestone, Nucl. Data Sheets **108**, 2319 (2007).
[32] C. D. Nesaraja and E. A. Mccutchan, Nucl. Data Sheets **133**, 1 (2016).
[33] E. Browne and J. K. Tuli, Nucl. Data Sheets **111**, 2425 (2010).
[34] J. Katakura and K. Kitao, Nucl. Data Sheets **97**, 765 (2002).
[35] M. J. Maetin, Nucl. Data Sheets **114**, 1497 (2013).
[36] T. Vidmar, Nucl. Instrum. Methods Phys. Res. A **550**, 603 (2005).
[37] T. Vidmar, G. Kanisch, and G. Vidmar, App. Radiat. Isot. **908**, 69 (2011).
[38] L. R. M. Punte *et al.*, Phys. Rev. C **95**, 024619 (2017).
[39] R. Pachuau *et al.*, Nucl. Phys. A **992**, 121613 (2019).
[40] D. W. Millsap and S. Landsberger, Appl. Radiat. Isot. **97**, 2 (2015).
[41] E. Robu and C. Giovani, Rom. Rep. Phys. **61**, 295 (2009).
[42] K. R. Jackman, Ph.D. dissertation submitted to the University of Texas at Austin, August, 2007.
[43] R. Nowotny, XMuDat: photon attenuation data on PC, IAEA Report No. IAEA-NDS 195 (1998).
[44] A. Iljinov *et al.*, Nucl. Phys. A **543**, 517 (1992).
[45] A. J. Koning and J. P. Delaroche, Nucl. Phys. A **713**, 231 (2003).
[46] R. Capote *et al.*, Nucl. Data Sheets **110**, 3107 (2009).
[47] G. R. Satchler, *Direct Nuclear Reactions* (Oxford University Press, New York, 1983).
[48] J. Raynal, Notes on ECIS94, CEA Saclay Report No. CEA-N-2772 (1994).
[49] C. Kalbach, Phys. Rev. C **33**, 818 (1986).
[50] P. A. Moldauer, Phys. Rev. C **14**, 764 (1976).
[51] P. A. Moldauer, Nucl. Phys. A **344**, 185 (1980).
[52] H. O. Menlove *et al.*, Phys. Rev. **163**, 1299 (1967).
[53] D. C. Santry and J. P. Butler, Can. J. Phys. **44**, 1183 (1966).